Long-Wavelength VCSEL Using High-Contrast Grating

Yi Rao, *Student Member, IEEE*, Weijian Yang, *Student Member, IEEE*, Christopher Chase, Michael C. Y. Huang,
D. Philip Worland, Salman Khaleghi, Mohammad Reza Chitgarha, Morteza Ziyadi,
Alan E. Willner, *Fellow, IEEE*, and Connie J. Chang-Hasnain, *Fellow, IEEE*

(Invited Paper)

Abstract—Recent advances in high-contrast grating (HCG) vertical-cavity surface-emitting lasers (VCSEL) emitting at 1550 nm is reported in this paper. The novel near-wavelength HCG has an ultrathin structure and broadband reflectivity. It enables a monolithic, simple fabrication process for realizing InP-based VCSELs emitting at ∼1550 nm. We report 2.4-mW single-mode output under continuous-wave operation at 15 °C. We show that, despite broadened by the Brownian motion, the HCG-VCSEL has a total linewidth of 60 MHz or a coherent length of 5 m in air, and an intrinsic linewidth <20 MHz. Transmission of directly modulated 10 Gbps over 100-km dispersion-compensated single-mode fiber is demonstrated. Tunable HCG-VCSEL is demonstrated with the HCG integrated with a micro-electro-mechanical structure. Continuous wavelength tuning as wide as 26.3 nm is achieved. The tunable VCSEL was used as a source for external modulation for 40-Gbps differential-phase-shift-keyed signal and transmitted over 100-km dispersion-compensated link with negligible power penalty.

Index Terms—High-contrast subwavelength grating, laser linewidth, optical MEMS, optical communication, vertical-cavity surface-emitting laser (VCSEL).

I. INTRODUCTION

VERTICAL-cavity surface-emitting lasers (VCSELs) are key optical sources in optical communications, the dominant source deployed in local area networks using multimode optical fibers at 850 nm. The advantages of VCSELs include wafer-scale testing, low-cost packaging, and ease of fabrication into arrays. The ease of array fabrication is partic-

Y. Rao, W. Yang, and C. J. Chang-Hasnain are with the Department of Electrical Engineering and Computer Sciences, University of California at Berkeley, Berkeley, CA 94704 USA (e-mail: cch@eecs.berkeley.edu).

C. Chase, M. C. Y. Huang, and D. P. Worland are with Bandwidth10, Inc., San Jose, CA 94063 USA.

S. Khaleghi, M. R. Chitgarha, M. Ziyadi, and A. E. Willner are with the Department of Electrical Engineering, University of Southern California, Los Angeles, CA 90089 USA.

ularly useful for space-division-multiplexed (SDM) links using multicore fiber or fiber arrays. VCSELs emitting in the 1.3–1.6 μm wavelength regime, also known as long-wavelength VCSELs, are highly desirable for the rising applications of data and computer communications, in addition to optical access networks, optical interconnects, and optical communication among wireless base stations. The potential advantages over conventional distributed feedback (DFB) and distributed Bragg reflector (DBR) lasers include much lower cost due to smaller footprint and wafer-scale testing, and significantly lower power consumption [1]. InP-based long-wavelength VCSELs have been demonstrated using techniques such as metamorphic GaAs DBR [2], buried tunnel junction [3], [4], substrate removal [5], and multisteps wafer fusion [6], [7] in the last ten years. However, all of these solutions require complex, expensive manufacturing processes. To date, long-wavelength InP-based VCSELs have not made major inroads on the market. Designing a device structure that can be manufactured as cost-effective as 850-nm GaAs-based VCSELs remains a major challenge.

Tunable light sources are important for wavelength division multiplexing (WDM) systems with applications including sparing, hot backup, and fixed wavelength laser replacement for inventory reduction [8]. They give network designers another degree of flexibility to drive down overall system cost. Such considerations are especially important for fiber-to-the-home and data center applications. Additionally, mode-hop-free, fast and widely tunable light sources are a perfect candidate for optical coherent tomography (OCT) [9] and light ranging applications [10]. Tunable VCSELs using micro-electro-mechanical structures (MEMS) are desirable because of their continuous tuning characteristics, making them promising for low-cost manufacturing and low-power consumption [11]. Although many structures have been reported with wide, continuous tuning range [9], [12], [13], largely due to their fabrication complexity, low-cost tunable 1550-nm VCSELs have not yet been available on the market.

In this paper, we report the first high-speed 1550-nm VCSEL and tunable VCSEL using a high-contrast grating (HCG) as the top mirror. A planar process of proton implant is used to provide current confinement, leading to a wafer-scale, low-cost fabrication process. Direct modulation up to 10 Gbps and transmission over a 100-km dispersion-compensated single-mode fiber (SMF) link are demonstrated using an HCG-VCSEL.

Fig. 1.   (a) Schematic of the HCG structure. The grating is comprised of dielectric bars of high refractive index, surrounded by a low index medium. The input wave is surface-normal incident from the top along k_0. Λ, HCG period; s, bar width; a, air gap width; t_g, HCG thickness. Duty cycle $\eta = s/\Lambda$. The reflectivity spectrum for (b) TE-HCG and (c) TM-HCG is calculated with HCG analytical solution [16]–[18]. The optimized TE-HCG has a very high reflectivity for E-field along the y-direction, but significantly lower along x-direction. The opposite is true for TM-HCG, and this enables polarization selection in HCG-VCSELs.

Tunable HCG-VCSELs show a continuous tuning range of 26.3 nm with >1.4-mW single-mode output under room temperature continuous-wave (CW) operation over most of the tuning range.

MEMS-based tunable VCSELs had previously been shown to exhibit broadened linewidths typically on the order of a few hundreds of megahertz to gigahertz due to mechanical fluctuation of MEMS caused by the Brownian motion [14], [15]. This could be problematic for applications requiring laser coherence linewidth < 100 MHz or length >3 m in free space. In this paper, we investigate this particular issue using self-heterodyne measurement with various delay lengths, and provide a new perspective to the linewidth of the HCG and MEMS VCSEL. We show that a 60 MHz total linewidth and a <20-MHz intrinsic linewidth are extracted from the measurements for the first time. In addition, using the tunable VCSEL as a CW source for external modulation, we demonstrated error-free transmission of 40-Gbps differential-phase-shift-keyed (DPSK) signals through a dispersion-compensated 100-km SMF link.

This paper is organized as follows. The basic concept of HCG is briefly reviewed, followed by the design, fabrication, and characteristics of HCG-VCSELs under CW operation. We then discuss the linewidth measurement of the HCG-VCSEL. Next, we discuss the design, fabrication, and electrical and optical characteristics of high speed directly modulated VCSELs and tunable VCSELs. Finally, we show the transmission measurements using the tunable VCSEL as a CW source for an external modulator.

II. CONCEPT OF HIGH-CONTRAST GRATING

The HCG is a single layer of near-wavelength grating consisting of high refractive-index material grating bars fully surrounded by low-index materials, shown in Fig. 1(a) [16]–[18]. By near-wavelength, we mean that the grating period is bounded by the limits of one wavelength in air and the high-index medium

[18]. This unique dimension constraint and refractive-index contrast results in extraordinary properties [18]. In this particular case for VCSELs, we design the HCG to exhibit broadband, high reflectivity for surface-normal incident light with polarization either parallel or orthogonal to the gratings (y-direction), also known as transverse electric (TE), and transverse magnetic (TM) light, respectively. Fig. 1(b) and (c) shows the surface normal reflection spectrum of a TE-HCG and TM-HCG calculated with the HCG analytical solution [16]–[18]. The HCG reflectivity, shown in Fig. 1(b), is optimized for TE-polarization (>99% reflectivity over a more than 100-nm wavelength range). In contrast, when the HCG is optimized for TM-polarization, shown in Fig. 1(c), the TM-polarization has 99% reflectivity over 150 nm. In either case, the reflectivity of the other polarization is low. As shown in the later section, this reflectivity difference can descriminate different polarization modes, and thus polarization mode selection in HCG-VCSELs is easy and flexible. In addition, the reflectivity of HCG at a specific wavelength range can be designed by varying the duty cycle, period, and thickness of HCG, so that arbitrary reflectivity between 98% and 100% can be achieved by different grating design [19].

To understand the broadband high reflectivity phenomenon, the electromagnetic field profile inside the grating can neither be approximated nor ignored. Recently, we published a simple analytic formulism to explain the broadband high reflection [16]–[18]. Here we provide a brief review.

The grating bars can be considered as a periodic array of waveguides along the z-direction. Upon plane wave incidence, only a few waveguide array modes are excited. Due to a large-index contrast and near-wavelength dimensions, there exists a wide wavelength range where only two modes have real propagation constants in the z-direction and, hence, carry energy. This is the regime of interest, and is referred as the *dual-mode* regime. The two modes then depart from the grating input plane ($z = 0$) and propagate downward ($+z$-direction) to the grating output plane ($z = t_g$), and then reflect back up. If the HCG is properly designed such that the two modes carry similar energy but opposite phases at the HCG output plane, destructive interference occurs. This cancels the transmission and thus all of the power must be reflected. Note that only the zeroth diffraction order carries energy due to the subwavelength period in air. The broadband property is attributed by the high-index contrast between the grating bars and the surrounding medium.

Fig. 2 shows the reflectivity contour plot of the TE- and TM-HCG versus normalized wavelength and grating thickness (both normalized by Λ). A well-behaved, highly ordered, checker-board pattern reveals its strong property dependence on both wavelength and HCG thickness, which indicates an interference effect. This checker-board pattern is particularly pronounced in the *dual-mode* regime, where there are only two propagation modes in HCG. The Fabry–Perot resonance conditions of these two modes are shown by the white curves. A detailed and comprehensive explanation of HCG physics can be found in [18].

Based on Fig. 2, one can locate the high reflectivity regions for an HCG-VCSEL design. For TE-HCGs (duty cycle $\eta = 0.35$), the desirable t_g/Λ is ~0.2, and λ/Λ is ~1.5; while
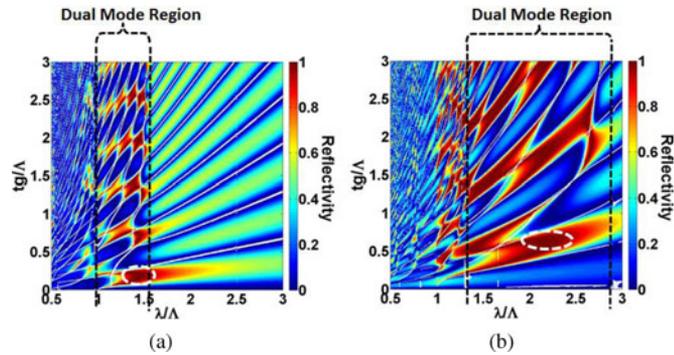
Fig. 2. Reflectivity contour plot of HCG versus normalized wavelength (λ/Λ) and normalized thickness (t_g/Λ) for (a) TE design with 35% duty cycle and (b) TM design with 65% duty cycle. The dual-mode region indicates the wavelength range where there are only two propagation modes in HCG. The white curves show the Fabry-Perot resonance conditions of these two modes. The circled area is the high reflectivity zone, where the HCG would be designed for the VCSEL. The refractive index for the HCG bar is 3.17.

Fig. 3. Cross-sectional schematic of a VCSEL with an HCG top mirror.

Fig. 4. *Left*: SEM image of a fabricated TE-HCG-VCSEL. The grating is aligned to the center of ring contact and mesa. *Right*: Zoomed-in SEM image shows the fully suspended HCG mirror surrounded by air.

Fig. 5. (a) Light-injection current–voltage (LIV) of a TE-HCG-VCSEL under CW operation from 15 to 85 °C. (b) Lasing spectrum at a fixed current of $4*I$th at different heat sink temperatures from 15 to 85 °C.

for TM-HCG ($\eta = 0.65$), the desirable t_g/Λ is ~0.6, and λ/Λ is ~2.2.

We experimentally demonstrated the broadband high reflectivity with an Si HCG on top of SiO_2 in 2004 [20]. In 2007, we applied this novel HCG concept on an 850-nm VCSEL [21], and demonstrated room temperature CW operation with an HCG reflectivity greater than 99%. Later, in 2008, we reported MEMS-tunable HCG-VCSELs with a 20-nm tuning range and 27-MHz tuning speed [22], [23]. The 1550-nm InP-based HCG-VCSEL was demonstrated in 2010 [24]. Many advances of HCG-VCSELs and lasers have been reported since 2008 [25]–[28]. In the following sections, we will focus on the discussion on 1550-nm HCG-VCSELs.

III. 1550-NM HCG-VCSEL DESIGN AND FABRICATION

The GaAs-based 850-nm VCSELs are manufactured cost-effectively in wafer-scale largely attributed to the fact that they can be made with one single epitaxy and simple device definition for current confinement. However, it has been difficult to fabricate long-wavelength VCSELs with one single epitaxy because of complex process needed for current confinement and challenges in obtaining high reflectivity DBR with high thermal conductance. Using an ultrathin HCG structure, we showed that a planar and monolithic process of proton implantation can be used to provide current confinement in 1550-nm HCG-VCSELs [24]. This is made possible because of the relatively thin thicknesses of the HCG and sacrificial layer. Additionally, a tunnel junction is used to minimize the amount of p-type materials, thus reducing the free carrier absorption and electrical resistance.

The schematic of an HCG-VCSEL lasing at 1550 nm is shown in Fig. 3, where the HCG grating is fully suspended in air. The as-grown epitaxial wafer consists of 40–55 pairs of bottom n-DBR, an active region, p-type cladding, tunnel junction, sacrificial layer, HCG layer, and top contact layer. The current aperture is defined by 300–400 keV H+ implant depending on the thickness of the sacrificial layer. The diameter of the current aperture
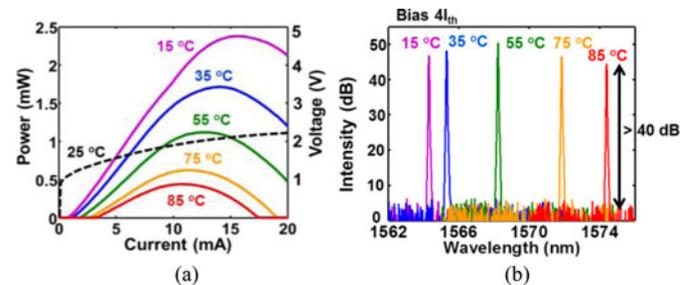
varies from 8 to 20 μm depending on the specific design. An annular top contact and uniform bottom contact are deposited by electron beam evaporation. After the formation of top and bottom contact, a mesa is defined by wet chemical etching, so the devices are electrically isolated from each other. The HCG is defined by electron beam lithography and followed by anisotropic vertical etching. Finally, the HCG structure is released by wet chemical etching and critical point drying. Scanning electron microscope (SEM) images of a completed HCG-VCSEL are shown in Fig. 4.

IV. CONTINUOUS-WAVE OPERATION OF THE 1550-NM HCG-VCSEL

The VCSELs have excellent CW performance characteristics. Fig. 5(a) shows the temperature dependent light–current–voltage (LIV) characteristic of a TE-HCG-VCSEL with continuous output power of 2.4 mW at 15 °C and 0.5 mW at 85 °C. The devices have slope efficiencies of ~0.25 mW/mA and threshold currents of <1 mA at 15 °C. The spectral characteristics are
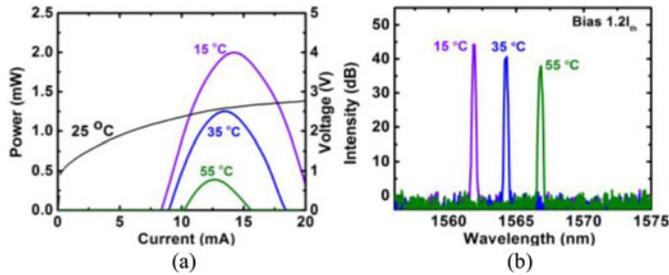
Fig. 6. (a) Light–current–voltage (LIV) of a TM-HCG-VCSEL under CW operation from 15 to 55 °C. (b) Lasing spectrum at fixed current of $1.2*I$th at different heat sink temperatures from 15 to 55 °C.

Fig. 7. Thermal characteristics of a 12-μm aperture device. (a) Wavelength shift versus heat sink temperature at a fixed bias current. (b) Wavelength shift versus dissipated power. Blue markers are the experimental data, fitted with the red solid curve.

shown in Fig. 5(b) with fixed bias current $I = 4I$th at different temperatures, which is a single polarization mode from 15 to 85 °C. The device has a bias voltage of 2.2 V at 20 mA, indicating 50–60 Ω of series resistance. The resistance could be further reduced by optimizing the doping level in the current spreading layer as well as the proton implant condition. The wall-plug efficiency is 10% at 15 °C, which is mainly limited by the relatively high voltage and series resistance.

Another unique property of the HCG-VCSEL is the single-mode preference. The VCSEL shown in Fig. 5 has an aperture size of 12 μm, which would be a multimode device in conventional VCSELs [5]. However, in the HCG-VCSEL case, the side-mode-suppression-ratio (SMSR) is >40 dB over the whole temperature range. The reason is that HCG has a greater angular dependence of reflectivity compared with DBR mirrors. Higher order modes, having smaller effective indexes or larger off-axis components of their wave vector, experience larger losses from the HCG mirror and are discriminated. Furthermore, large aperture single-mode emission with high-output power is possible with the HCG mirror.

The LIV characteristics of a TM-HCG-VCSEL are shown in Fig. 6. The TM-VCSEL has 2-mW output power at 15 °C, and 0.5 mW at 55 °C. The device has an SMSR >40 dB across the temperature range. Here the TM-HCG-VCSEL has higher threshold current, most likely due to process imperfection. In principle, TM-devices should have similar reflectivity as TE-devices, and the threshold current should be similarly low. Additionally, the high threshold current is the major factor preventing the device from working at higher temperatures.

To improve the VCSEL performance, it is critical to reduce its thermal resistance. For a single-mode VCSEL, proton-implanted gain-guided devices typically have 10–30 times larger current aperture than their index-guided counterparts. Hence, the thermal conductivity of a proton-implanted HCG-VCSEL is 10–30 times better. In the HCG-VCSEL reported here, despite a much worse thermal conductivity of the thick bottom DBR, our devices have similar or even better thermal conductivity compared with the buried-tunnel-junction (BTJ) VCSELs [5]. As shown in Fig. 7(a), the wavelength shift versus temperature is 0.102 nm/K. This number is determined by index change versus temperature. As shown in Fig. 7(b), the wavelength shift versus dissipated power is 0.162 nm/mW. By combining these two numbers, the thermal resistance of our device is ~1.59 K/mW.
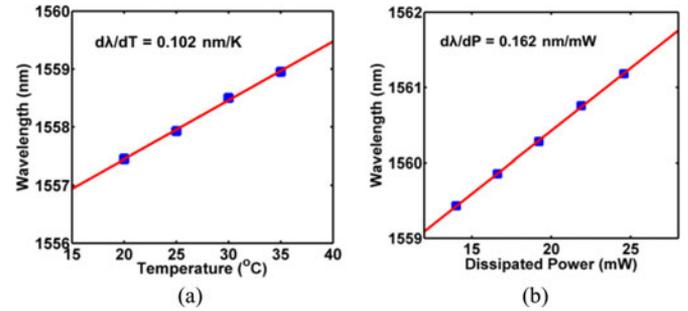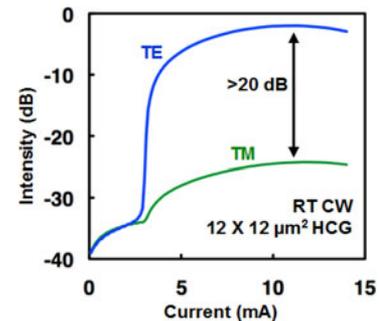
Fig. 8. Polarization-resolved light–current characteristics of a 1550-nm HCG VCSEL at room temperature (RT). A polarization suppression ratio of >20 dB is achieved with the measurement limited by the extinction ratio of the polarizer.

Favorable optical mode characteristics for optical communications applications are also obtained due to the use of HCG. An important characteristic for VCSELs for mid- and long-reach optical communication links is polarization stability, as any polarization instability can have detrimental effects on an optical link. For instance, in a conventional DBR VCSEL case, polarization mode-hopping happens frequently during modulation since there is no discrimination mechanism for different polarization modes. However, HCG-VCSELs are polarization stable due to the high differentiation between the reflectivity in the orthogonal electric field polarizations. Fig. 8 shows the polarization-resolved light-current characteristics of a device with a 15 μm proton implant aperture and $12 \times 12 \ \mu m^2$ size HCG. The orthogonal polarization is suppressed by >20 dB. The measurement is limited by the extinction ratio of the polarizer in the experimental setup.

V. LINEWIDTH OF HCG-VCSEL

The HCG is a single layer of suspended freely standing sub-wavelength grating serving as a top reflector for the VCSEL cavity. When combined with an actuator, this becomes an MEMS, which provides a wide, continuous wavelength tuning capability to VCSELs. The laser wavelength is changed by the variation of top mirror position relative to the cavity, as will be discussed in Section VII. On the other hand, such MEMS structure is prone to noise induced by the Brownian motion, which vibrates the mirror and changes the laser wavelength. This effectively

broadens the laser linewidth. The linewidth of MEMS VCSEL was reported previously to be very wide, typically on the order of a few hundreds of megahertz to gigahertz by self-heterodyning [15] or heterodyning with another tunable laser [14] and ~10–100 times larger than that of a typical single-wavelength VCSEL [14], [15]. The wide linewidth could present a major limitation on applications where the coherence of a laser source is of importance.

Here, we investigate the MEMS HCG-VCSEL linewidth with a new measurement scheme and provide a new perspective of the MEM VCSEL linewidth. First, we realize that the linewidth broadening must assume the same mechanical frequency response of the MEMS structure, with a resonance frequency in kilohertz to megahertz range depending on design. Hence, for light prorogation less than ms–μs, the meaningful laser linewidth can be much closer to the intrinsic laser linewidth, which is distinctly narrower than that obtained using heterodyne. In fact, the measurements using conventional self-heterodyne may be misleadingly wide when the fiber delay length is too long. In such measurements, the measured linewidth is dominated by the averaging effect due to Brownian motion. The intrinsic laser linewidth discussed here is referred to the laser linewidth without the Brownian motion induced broadening.

To investigate this effect and differentiate laser intrinsic and Brownian linewidth, we measure the self-heterodyne linewidth as a function of fiber delay length on one arm. The VCSEL's optical output is split into two arms. The light on one arm is modulated by a Mach–Zehnder modulator and delayed by time τ_d through a SMF. It is then combined with the light from the other arm at a photodetector, and the RF signal containing their beat notes is measured in an RF spectrum analyzer. In general, the profile of the laser's intrinsic linewidth ($\Delta\nu_i$) spectrum is Lorentzian. The Brownian motion of the HCG changes the length of the laser cavity and thus induces a frequency fluctuation, whose spectrum profile is Gaussian (with linewidth $\Delta\nu_B$). Thus, the profile of VCSEL linewidth ($\Delta\nu$) is a Voigt function, convolution of Lorentzian and Gaussian. By curve-fitting the measured spectrum, the Gaussian and Lorentzian terms can be separated. The laser's linewidth $\Delta\nu$ is estimated as the FWHM of the Voigt profile over $\sqrt{2}$, whereas the intrinsic linewidth $\Delta\nu_i$ is half of the FWHM of the Lorentzian term [15]. The measured Voigt profile of the HCG-VCSEL is dominated by the Gaussian term, indicating $\Delta\nu_B > \Delta\nu_i$. Fig. 9 shows the measured linewidth of 60 MHz, with VCSEL intrinsic linewidth $\Delta\nu_i < 20$ MHz (measured with a fiber delay length of ~49.6 m). Both are significantly less than the previously reported values. The corresponding coherent length for the HCG-VCSEL is 5 m in air considering both intrinsic linewidth and Brownian motion-induced broadening.

To study the Brownian motion-induced linewidth broadening, various lengths of fiber were used in the measurement, and the measured $\Delta\nu$ for three different VCSELs with different HCG mirror size is plotted versus the fiber delay length or the inversed fiber delay time ($1/\tau_d$) in Fig. 10. The HCG sizes are 12×12, 16×16, and 20×20 μm^2. The VCSEL powers are very similar emitting 0.5–1 mW. First of all, we note that the smallest HCG has a stiffest spring constant and is thus least prone to Brownian
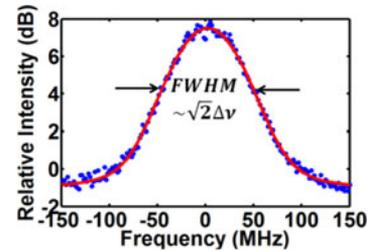
Fig. 9. Typical RF spectrum of the beat note of self-heterodyne linewidth measurement of an HCG-VCSEL with a fiber delay length of 49.6 m. The experimental data (blue dots) are fitted with Voigt profile (red curve). The laser's linewidth $\Delta\nu$ is estimated as the FWHM of the Voigt profile over $\sqrt{2}$. The total linewidth of this VCSEL is extracted to be 60 MHz, and the laser intrinsic linewidth to be <20 MHz.
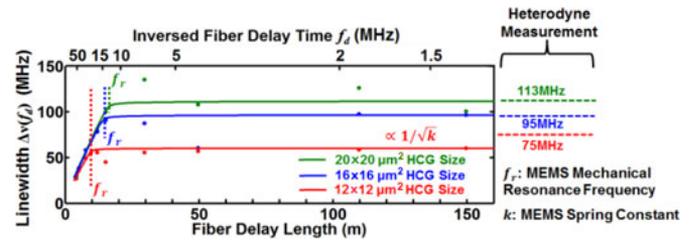
Fig. 10. HCG-VCSEL linewidth versus fiber delay length or inversed fiber delay time in self-heterodyne measurement, for three different VCSELs with different HCG mirror size. The experimental data (dots) are curve-fitted with the theoretical model (solid curves). The smaller HCG size has a stiffer spring and a higher mechanical resonance frequency (marked by f_r, the vertical dotted line); correspondingly, its linewidth reaches the saturation point at a shorter fiber delay length, and its final linewidth is smaller (proportional to $1/\sqrt{k}$). The delay-dependence self-heterodyne measurements are compared with heterodyne measurements using a tunable laser (Agilent 81640 A, 100-kHz linewidth) as heterodyne source. It is seen that the heterodyne measurements agree with the saturated values as fiber delay is very long.

noise, leading to a narrowest linewidth, with a value starting at ~40 MHz and increasing to 60 MHz with 150-m long fiber delay. For the larger HCG mirror size, the linewidth ranges from ~50 to ~130 MHz. We compared the delay-dependence self-heterodyne measurements with heterodyne measurements using a tunable laser (Agilent 81640 A, 100-kHz linewidth) as heterodyne source. We can clearly see that the heterodyne measurements agree with the saturated values as fiber delay is very long.

It is seen that $\Delta\nu$ increases with the fiber length until the fiber length reaches a certain value. This can be explained by the Brownian motion. As the fiber delay length increases, the delay time between the two arms increases, during which more and more Brownian motion accumulates and thus the linewidth gets broadened. Upon a certain fiber length, the delay time is long enough such that all the Brownian motions are fully exposed, and thus its influence on linewidth no longer increases with any further increase of fiber delay. To better understand this, we examine the Brownian motion's power spectrum density, and theoretically model this linewidth broadening. The HCG's displacement spectrum $X(f)$ can be expressed as

$$X(f) = F(f)H(f) \tag{1}$$

where $H(f)$ is the MEMS transfer function and $F(f)$ is noise force spectrum. The noise force can be considered as white noise, and thus $F(f) = F_n$. The total root-mean-square (rms) displacement x_{rms} due to Brownian motion can thus be expressed as [14]

$$x_{\text{rms}}^2 = \int_0^\infty F_n^2 H(f)^2 \, df. \qquad (2)$$

On the other hand, the energy that the MEMS HCG stores $(1/2)kx_{\text{rms}}^2$ equals to the thermal energy $(1/2)k_bT$, where k is the spring constant of the HCG, k_b is the Boltzmann constant, and T is the temperature. Thus, we have

$$x_{\text{rms}} = \sqrt{\frac{k_bT}{k}}. \qquad (3)$$

By relating (2) and (3), F_n can be solved.

In the self-heterodyne measurement, the light in one path is delayed by τ_d with respect to the other. All the frequency fluctuation that happened within τ_d will contribute to the linewidth broadening. Thus, all the Brownian motion with frequency $f > f_d = 1/\tau_d$ will have full contributions to the broadening, while those with frequency $f < f_d$ will partially contribute. As a first order of approximation, we use the following weight factor to describe their contribution

$$\begin{cases} 1, & f > f_d \\ f/f_d, & f < f_d. \end{cases} \qquad (4)$$

Thus, the x_{rms} for a specific f_d can be expressed as

$$|x_{\text{rms}}(f_d)|^2 = \int_0^{f_d} \left| \frac{f}{f_d} X(f) \right|^2 df + \int_{f_d}^\infty |X(f)|^2 \, df. \qquad (5)$$

The rms frequency fluctuation $\Delta\nu_{\text{rms}}(f_d)$ can then be calculated based on the free spectrum range of the VCSEL cavity, as well as the detailed MEMS which translates the overall displacement into frequency fluctuation. $\Delta\nu_B(f_d)$ can then be expressed as

$$\Delta\nu_B(f_d) = 2\sqrt{(2\ln 2)\Delta\nu_{\text{rms}}^2(f_d)}. \qquad (6)$$

The laser's average linewidth $\Delta\nu(f_d)$ can then be calculated with the following formula which relates the FWHM of the Voigt profile with the FWHM of its Lorentzian and Gaussian component:

$$\Delta\nu(f_d) = 0.5346\Delta\nu_i + \sqrt{0.2166\Delta\nu_i^2 + \Delta\nu_B(f_d)^2}. \qquad (7)$$

There are several characteristics of $\Delta\nu(f_d)$. First, $\Delta\nu(f_d)$ increases as f_d decreases. When $f_d < f_r$, $\Delta\nu(f_d)$ gets saturated. Thus, the MEMS mechanical resonance frequency f_r can be characterized by this measurement. Second, the final $\Delta\nu$ ($f_d < f_r$) is mainly determined by the spring constant of the MEMS mirror. In the case when the Brownian motion induced linewidth broadening dominates the total linewidth, i.e., $\Delta\nu_B \gg \Delta\nu_i$, $\Delta\nu$ can be expressed as the following formula:

$$\Delta\nu(f_d < f_r) \approx \Delta\nu_B(f_d < f_r) \approx 2.35a_0 \frac{2c|\Delta\lambda_{\text{FSR}}|}{\lambda_0^3} \sqrt{\frac{k_bT_0}{k}}$$
$$\qquad (8)$$

where $\Delta\lambda_{\text{FSR}}$ is the free spectrum range of the VCSEL, λ_0 is the laser wavelength in vacuum, and c is the speed of light in vacuum. This formula is similar as the one reported in [15], but with an extra factor a_0 which depends on the detailed MEMS structure. $a_0 = 1$ when the whole MEMS mirror can be uniformly actuated.

The experimental data are compared with calculations using the aforementioned formulism, as shown in Fig. 10. Excellent agreement is obtained. The smaller HCG size has a stiffer spring and a higher mechanical resonance frequency; correspondingly, its linewidth reaches the saturation point at a shorter fiber delay length, and its final linewidth is smaller. The intrinsic linewidth is extracted to be <20 MHz.

The aforesaid experiment is performed with a nontunable HCG-VCSEL. The spring constant for the tunable HCG-VCSEL is typically smaller leading to a larger Brownian-motion induced broadening. However, the linewidth of a tunable VCSEL could in principle approach the measured results here. This experiment and theoretical modeling provides a new perspective of the MEMs VCSEL linewidth. We believe with optimized spring constant, the Brownian-motion induced linewidth broadening can be greatly reduced to ∼10 MHz. For applications in OCT or light detection and ranging (LIDAR), this Brownian motion induced linewidth broadening may not affect the ranging performance depending on the distance of interests. At short fiber delay lengths, the influence of the Brownian motion is not much. This opens up many applications using tunable VCSELs as an optical swept source.

VI. HIGH-SPEED DIRECT MODULATED HCG-VCSEL

Reducing the parasitic RC and optimizing thermal design are key factors for the HCG-VCSEL to go beyond 10 Gbps under direct electrical modulation. By shrinking the size of mesa, parasitic capacitance can be reduced. On the other hand, this may adversely impact device performance with increased thermal and electrical resistances. With careful optimization, we achieved a high-speed TE-HCG-VCSEL with 2.2-mW output power, and 4.3-mA threshold current at room temperature using a 40×40 μm^2 mesa. The small signal modulation response (S21) of the VCSEL is shown in Fig. 11. A 3-dB bandwidth of 7.8 GHz is obtained at $2.5I$th bias curent. The fitted capacitance of the 40×40 μm^2 mesa device is 0.606 pF, and the measured resistance is $60\,\Omega$, which indicates a parasitic cutoff frequency of 4.38 GHz. Therefore, the device performance is still limited by parasitic capacitance, which can be further reduced by shrinking the mesa size to 30×30 μm^2 and two steps proton implant. Ultimately, 15-GHz patrasitic RC bandwidth is achievable.

The D-factor of this device is around 3.7 GHz/mA$^{1/2}$, and the maximum resonance frequency is 7.4 GHz, shown in Fig. 12. The kink in the linear fitting curve is due to the thermal damping effect that happens at 11 mA bias current. Usually, the 3-dB bandwidth is 1.5 times of resonance frequency, but here they are roughly the same. This provides further evidence that the device is parasitic RC-limited. The relatively small D-factor is due to the large current aperture, and the long cavity length due to the large penetration depth into bottom DBR. It can be further
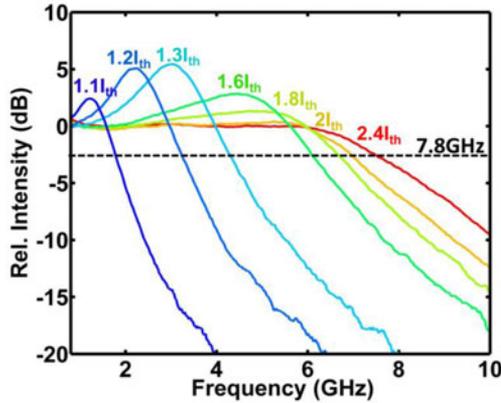
Fig. 11.   S21 small signal response with different bias current, the maximum 3 dB bandwidth is 7.8 GHz, which is limited by parasitic capacitance.
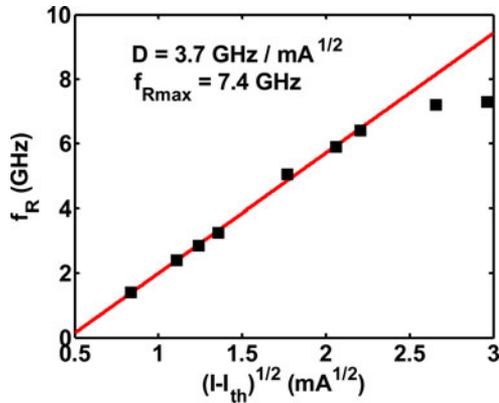
Fig. 12.   D-factor fitting from resonance frequency versus bias current, a device with $40 \times 40~\mu m^2$ mesa size has a D-factor of 3.7 GHz/mA$^{-1/2}$, and the max resonance frequency is 7.4 GHz after thermal damping. Black markers show the experimental results, fitted by the red solid curve.

improved with a shorter cavity design. The thermal damping of the D-factor happens at around 11 mA, which is a large number for single-mode VCSELs. Considering that the bottom DBR stack has one order of magnitude worse thermal conductivity than InP, this result actually indicates that the large aperture induced by proton implant really helps the thermal performance of the device. To further increase the 3-dB bandwidth of S21 response, larger D-factor is desirable, which can be achieved by reducing the aperture size, fine tuning the HCG reflectivity, and increasing the strain in quantum wells. Given that HCG is just a replacement of the reflectors compared to DBR VCSELS, HCG-VCSELs should have the same high-speed modulation potential as other DBR VCSELs [4]–[6], yet further improvement of design and process is needed to extend the bandwidth.

Fig. 13 shows the eye diagrams and BER curves of a direct On–Off-key (OOK) modulated TE-HCG-VCSEL. The device has error-free (BER $< 10^{-9}$) operation up to 10 Gb/s at 20 °C. Fiber transmission performance of the signal was assessed using bit-error-rate (BER) measurements before (back-to-back) and after transmission through a link consisting of 80-km SMF followed by 20 km of ~ -1378-ps/nm dispersion-compensated fiber (DCF) (Lucent DK-80). The BER after fiber transmission is
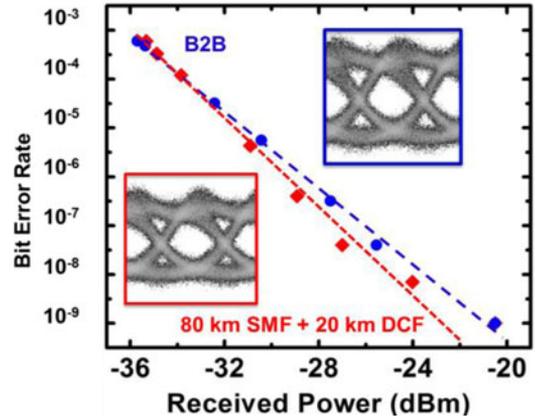
Fig. 13.   Eye diagrams and BER measurement of 10-Gb/s OOK directly modulated VCSEL: back-to back (B2B) (blue) and after transmission through a dispersion-compensated 100-km optical fiber link (red).
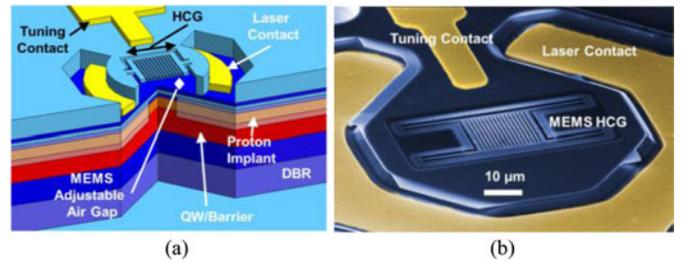
Fig. 14.   (a) Schematic of an MEMS tunable HCG-VCSEL, with an MEMS contact and laser contact to tune the HCG down electrostatically. (b) SEM image of an MEMS tunable HCG-VCSEL with bridge-type MEMS.

slightly better than back-to-back (B2B) which could result from the interactions of residual chromatic dispersion and chirp. The highest modulation speed is measurement equipment limited. Since our device is parastic RC limited, and the 3-dB bandwidth is 7.8 GHz, we believe that 12.5-Gbps direct modulation is achievable with these devices.

VII. Continuous Tunable HCG-VCSEL

The schematic and SEM image of a MEMS-tunable TE-HCG-VCSEL is shown in Fig. 14. The device stucture is very similar to the fixed wavelength devices in Fig. 3, except that HCG is now attached to a MEMS actuator. A tuning contact is formed on top of an electrically isolated junction. The HCG structure and the semiconductor layer beneath it act as a parallel capacitor transducer, and the HCG moves down with voltage applied between the tuning contact and laser contact. Therefore, the lasing wavelength tunes by varying the cavity length of VCSEL.

The tuning range of the tunable laser is shown in Fig. 15. The tuning range is 26.3 nm in total, including a 16.5 nm of mechanical tuning, and a 9.8 nm of current-induced thermal tuning. The mechanical tuning range can be further improved by predetuning the cavity peak to the longer wavelength side of the gain peak. The 9.8-nm thermal tuning shows that the gain region, mirror reflectivity, and confinement factor are strong enough to support the full 26.3-nm mechanical tuning. The VCSEL shows single-mode emission across the whole tuning range.
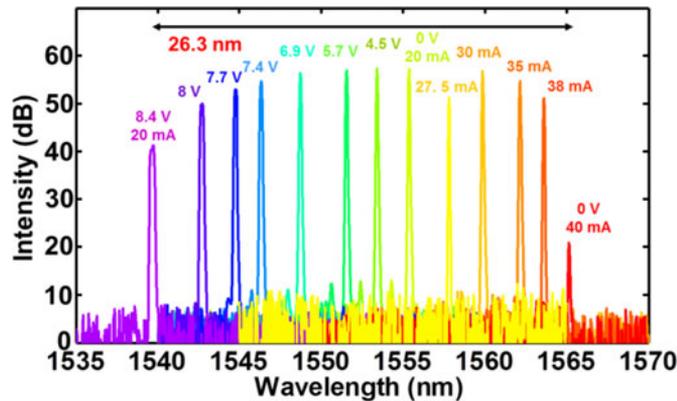
Fig. 15.   Tuning range of an MEMS tunable HCG-VCSEL under room temperature, CW operation. The laser lases over a range of 26.3 nm, where 16.3 nm is MEMs mechanical tuning, and 9.8 nm is thermal tuning.

Fig. 17.   Lasing wavelength versus tuning voltage, the black dotted line is the measurement results. This is well matched with the red line, which is simulated with the HCG dimension measured by SEM.
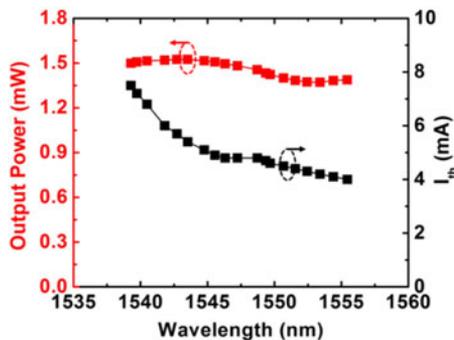
Fig. 16.   Maximum output power (red) and threshold current (black) as a function of the wavelength at 20 mA under room temperature CW operation. The device outputs over 1.4 mW over the whole mechanical tuning range.

Additionally, the tuning voltage (<10 V) is relatively small compared with other surface-machined tunable VCSELs [7], [9], [12] because of the light weight of HCG, which can also be integrated with CMOS electronics. Potentially it can also have a very fast tuning speed. The resonance frequency is proportional to $(k/m)^{1/2}$, where k is the spring constant, and m is the mass of the ultralight weight HCG.

As shown in Fig. 16, the maximum output power is more than 1.4 mW over the whole 16 nm of mechanical tuning range, and the threshold current is less than 5 mA over 10 nm of the tuning range, which indicates that the confinement factor, material gain, and HCG reflectivity are quite stable across the whole tuning range. The increasing threshold current versus wavelength is caused by larger gain-cavity detuing and thus higher threshold carrier density. It is noted that the lowest threshold is at the beginning of the tuning range, i.e., 1557 nm, indicating that at least half of the gain spectrum is not utilized. With better optimization of the initial cavity-gain detuing, a doubling of the tuning range, or up to 32-nm mechanical tuning is expected.

When applying tuning voltage to the device, the electrostatic force and elastic force from the MEMS spring will find a new equilibrium place which is lower than the original position. The relationship between tuning voltage and lasing wavelength follows approximately the power of 3/2 rules, and the maximum displacement of a parallel capacitor transducer is 1/3 of the air-

gap. The HCG mirror will be clamped down directly after moving downward by 1/3 of the airgap, which is roughly 9 V in this case. The relationship between tuning voltage and wavelength tuning is shown in Fig. 17. The black dotted line (measurement) matches the red line (simulation) well, which indicates that the HCG MEMS actuator behaves similarly to a micro-scale parallel plate capacitive transducer. In addition, due to the ultrathin thickness of the HCG mirror, the maximum tuning range can be achieved with ~8.5 V. The tuning efficiency is ~0.04 nm/nm, which means the lasing wavelength will change 0.04 nm if the length of the cavity gets reduced by 1 nm. The relative small tuning efficiency is due to relative large penetration depth into bottom DBRs.
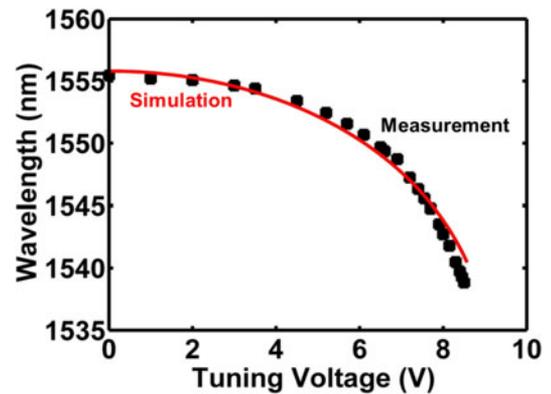
The wavelength tuning speed of the HCG MEMS actuator is mainly determined by the mechanical resonance frequency of the HCG, which currently has 3-dB bandwidth of 2.5 MHz. The speed of MEMS goes up linearly versus the volume of the structure, so small HCG, which is three orders of magnitude smaller than that in [12] potentially can have tuning speed up to 10–100 MHz, which is shown in [22]. In addition, more than 10 MHz of resonance frequency is demonstrated in the linewidth measurement in Section V, which further proves the ultrahigh tuning speed capability of HCG tunable VCSEL. This ultrahigh tuning speed will facilitate its application in the swept-source OCT, whose scanning speed can be improved 100 times compared with the swept sources that are currently being used [9], [29], [30].

To test the feasibility of the tunable HCG-VCSEL as a light source for optical communication, we demonstrated external modulation with the tunable devices. In this case, a tunable TE-HCG-VCSEL was used as a source for external modulation. A 40-Gbps pseudo-random bit sequence (PRBS) of length $2^{31}-1$ was used to drive an IQ modulator to generate a DPSK signal. At the receiver, the DPSK signal was sent into a 40-GHz-FSR delay-line-interferometer for balanced direct detection. Fiber transmission performance of the signal was assessed using BER measurements before (back-to-back) and after transmission through a dispersion-compensated 100-km fiber link. The compensated link included 80-km SMF followed by an EDFA and a spool of 20 km $\sim$$-1378$-ps/nm DCF (Lucent
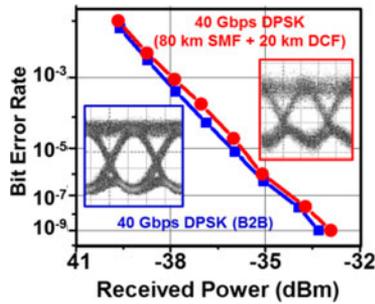
Fig. 18. Bit-error-rate measurements and eye diagrams for transmission of VCSEL 40-Gbps DPSK B2B (blue line) and through a dispersion-compensated 100-km SMF link with direct detection (red line).

DK-80). As can be seen in Fig. 18, there was a negligible power penalty after fiber transmission of the VCSEL signal.

VIII. CONCLUSION

The single-layer ultrathin and light-weight HCG with broadband high reflectivity enables monolithic and simple fabrication of an InP-based VCSEL lasing at 1550 nm. The fundamental physics of the HCG mirror has been analytically studied, and the anomalous high reflection broadband characteristic is explained in the *dual-mode* regime, which opens the door to better design and using HCG as a broadband reflector or other basic optical components.

With the innovative top mirror design, we have experimentally demonstrated CW operation TE- and TM-HCG-VCSELs lasing at 1550-nm with over 2-mW output power, respectively. Combined with a current aperture defined by proton implant, excellent thermal conductivity of 1.59 K/mW has been reported. The HCG-VCSEL lases up to 85 °C with 0.5 mW of output power. The measured >20-dB polarization-mode suppression ratio confirms the single polarization-mode lasing of HCG-VCSEL, which is desirable for high speed, polarization-mode-hop-free applications.

Brownian motion induced linewidth broadening is measured and studied, and the linewidth broadening of the device was found to increase with increasing delay length in the interferometer until it reaches a saturation value. The total linewidth of the device was ∼60 MHz, which indicates a coherent length of 5 μm in air. Further suppression of Brownian motion could be achieved by stiffer MEMS structure or a wavelength-stabilized feedback loop.

High speed directly modulated HCG-VCSELs were shown with 7.8 GHz of 3-dB bandwidth in their S21, and 10-Gbps large signal operation. Though the cutoff frequency of parasitic RC was increased to 4.38 GHz, the high-speed modulation was still limited by parasitics. Even higher modulation speed can be achieved by further reducing the mesa size and optimizing the bottom DBR.

MEMS tunable HCG-VCSELs with a 26.3-nm tuning range were demonstrated with an output power greater than 1.4 mW over 16 nm of tuning range. Thanks to its light weight, 100 times faster wavelength sweeping than the swept sources currently used in OCT [9], [29], [30] is achievable, which potentially

can facilitate ultrafast scanning rate in OCT and light ranging applications. In addition, we have demonstrated 40-Gbps DPSK over a fiber link with the tunable HCG-VCSEL.

The flexible, light-weight, monolithic HCG simplifies the process of InP-based VCSELs drastically and enables unique features, such as polarization mode selection, fast wavelength tuning, and a single transverse mode that other conventional approaches do not have. Therefore, the simplicity, wavelength-scalability, and versatility of the HCG would benefit numerous lightwave devices over different wavelength ranges and device structures.

REFERENCES

[1] C. J. Chang-Hasnain, J. P. Harbison, C. E. Zah, M. W. Maeda, L. T. Florez, N. G. Stoffel, and T. P. Lee, "Multiple wavelength tunable surface emitting laser arrays," *IEEE J. Quantum Electron.*, vol. 27, no. 6, pp. 1368–1376, Jun. 1991.

[2] W. Yuen, G. S. Li, R. F. Nabiev, J. Boucart, P. Kner, R. J. Stone, D. Zhang, M. Beaudoin, T. Zheng, C. He, K. Yu, M. Jansen, D. P. Worland, and C. J. Chang-Hasnain, "High-performance 1.6 μm single-epitaxy top-emitting VCSEL," *Electron. Lett.*, vol. 36, pp. 1121–1123, 2000.

[3] S. Baydar, K. Windhorn, G. Bohm, J. Rosskopf, R. Shau, E. Ronneberg, W. Hofmann, and M.-C. Amann, "2.5-mW single-mode operation of 1.55-μm buried tunnel junction VCSELs," *IEEE Photon. Tech. Lett.*, vol. 17, no. 8, pp. 1956–1958, Aug. 2005.

[4] N. Nishiyama, C. Caneau, G. Guryanov, X. S. Liu, M. Hu, and C. E. Zah, "High efficiency long wavelength VCSEL on InP grown by MOCVD," *Electron. Lett.*, vol. 39, pp. 437–439, 2003.

[5] M. C. Amann and W. Hofmann, "InP-based long-wavelength VCSELs and VCSEL arrays," *IEEE J. Selected Topic Quantum Electron.*, vol. 15, no. 3, pp. 861–868, May 2009.

[6] A. Mircea, A. Mereuta, A. Caliman, C.-A. Berseth, G. Suruceanu, V. Iakovlev, M. Achtenhagen, A. Rudra, and E. Kapon, "1.5-mW single-mode operation of wafer-fused 1550-nm VCSELs," *IEEE Photon. Tech. Lett.*, vol. 16, no. 5, pp. 1230–1232, May 2004.

[7] V. Jayaraman, M. Mehta, A. W. Jackson, S. Wu, Y. Okuno, J. Piprek, and J. E. Bowers, "High-power 1320-nm wafer-bonded VCSELs with tunnel junctions," *IEEE Photon. Tech. Lett.*, vol. 15, no. 11, pp. 1495–1497, Nov. 2003.

[8] V. Jayaraman, Z. M. Chuang, and L. A. Coldren, "Theory, design, and performance of extended tuning range semiconductor lasers with sampled gratings," *IEEE J. Quantum Electron.*, vol. 29, no. 6, pp. 1824–1834, Jun. 1993.

[9] B. Potsaid, V. Jayaraman, J. G. Fujimoto, J. Jiang, P. J. S. Heim, and A. E. Cable, "MEMS tunable VCSEL light source for ultrahigh speed 60 kHz–1 MHz axial scan rate and long range centimeter class OCT imaging," *Proc. SPIE*, vol. 8213, pp. 82130M–82130M-8, 2012.

[10] N. Satyan, A. Vasilyev, G. Rakuljic, V. Leyva, and A. Yariv, "Precise control of broadband frequency chirps using optoelectronic feedback," *Opt. Express*, vol. 17, pp. 15991–15999, 2009.

[11] C. J. Chang-Hasnain, "Tunable VCSEL," *IEEE J. Selected Topics Quantum Electron.*, vol. 6, no. 6, pp. 978–987, Dec. 2000.

[12] C. Gierl, T. Gruendl, P. Debernardi, K. Zogal, C. Grasse, H. A. Davani, G. Böhm, S. Jatta, F. Küppers, P. Meißner, and M.-C. Amann, "Surface micromachined tunable 1.55 μm-VCSEL with 102 nm continuous single-mode tuning," *Optics Express.*, vol. 19, pp. 17366–17343, 2011.

[13] T. Yano, H. Saitou, N. Kanbara, R. Noda, S. I. Tezuka, N. Fujimura, M. Ooyama, T. Watanabe, T. Hirata, and N. Nishiyama, "Wavelength modulation over 500 kHz of micromechanically tunable InP-based VCSELs with Si-MEMS technology," *IEEE J. Select. Topic Quantum Electron.*, vol. 15, no. 3, pp. 528–534, May 2009.

[14] D. Huber, P. Corredoura, S. Lester, V. Robbins, and L. Kamas, "Reducing Brownian motion in an electrostatically tunable MEMS laser," *J. Micro-electromech. Syst.*, vol. 13, pp. 732–736, 2004.

[15] H. Halbritter, C. Sydlo, B. Kögel, F. Riemenschneider, H. L. Hartnagel, and P. Meissner, "Impact of micromechanics on the linewidth and chirp performance of MEMS-VCSELs," *IEEE J. Select. Topic Quantum Electron.*, vol. 13, no. 2, pp. 367–373, Mar./Apr. 2007.

[16] V. Karagodsky, F. G. Sedgwick, and C. J. Chang-Hasnain, "Theoretical analysis of subwavelength high contrast grating reflectors," *Opt. Express.*, vol. 18, pp. 16973–16988, 2010.

[17] V. Karagodsky and C. J. Chang-Hasnain, "Physics of near-wavelength high contrast gratings," *Opt. Express.*, vol. 20, pp. 10888–10895, 2012.

[18] C. J. Chang-Hasnain and W. Yang, "High-contrast gratings for integrated optoelectronics," *Adv. Opt. Photon.*, vol. 4, pp. 379–440, 2012.

[19] T. Sun, W. Yang, Y. Rao, and C. J. Chang-Hasnain, "Experimental characterization on high contrast grating reflectivity," in *Proc. IEEE Photonics Conf.*, 2012, pp. 198–199.

[20] C. F. R. Mateus, M. C. Y. Huang, L. Chen, C. J. Chang-Hasnain, and Y. Suzuki, "Broad-band mirror (1.12–1.62 μm) using a subwavelength grating," *IEEE Photon. Tech. Lett.*, vol. 16, no. 7, pp. 1676–1678, Jul. 2004.

[21] M. C. Y. Huang, Y. Zhou, and C. J. Chang-Hasnain, "A surface-emitting laser incorporating a high-index-contrast subwavelength grating," *Nature Photonics*, vol. 1, pp. 119–122, 2007.

[22] C. Chase, Y. Zhou, and C. J. Chang-Hasnain, "Size effect of high contrast gratings in VCSELs," *Optics Express*, vol. 17, pp. 24002–24007, 2009.

[23] M. C. Y. Huang, Y. Zhou, and C. J. Chang-Hasnain, "A nanoelectromechanical tunable laser," *Nature Photonics*, vol. 2, pp. 180–184, 2008.

[24] C. Chase, Y. Rao, W. Hofmann, and C. J. Chang-Hasnain, "1550 nm high contrast grating VCSEL," *Optics Express*, vol. 18, pp. 15461–15466, 2010.

[25] I.-S. Chuang, J. Mork, P. Gilet, and A. Chelnokov, "Subwavelength grating-mirror VCSEL with a thin oxide gap," *IEEE Photon. Tech. Lett.*, vol. 20, no. 2, pp. 105–107, Jan. 2008.

[26] T. Stoferle, N. Moll, T. Wahlbrink, J. Bolten, T. Mollenhauer, U. Scherf, and R. F. Mahrt, "Ultracompact silicon/polymer laser with an absorption-insensitive nanophotonic resonator," *Nano Lett.*, vol. 10, pp. 3675–3678, Aug. 2010.

[27] I.-S. Chung, V. Iakovlev, A. Sirbu, A. Mereuta, A. Caliman, E. Kapon, and J. Mork, "Broadband MEMS-tunable high-index-contrast subwavelength grating long-wavelength VCSEL," *IEEE J. Quantum Electron.*, vol. 46, no. 9, pp. 1245–1253, Sep. 2010.

[28] C. Sciancalepore, B. B. Bakir, C. Seassal, X. Letartre, J. Harduin, N. Olivier, J.-M. Fedeli, and P. Viktorovitch, "Thermal, modal, and polarization features of double photonic crystal vertical-cavity surface-emitting lasers," *IEEE Photon. J.*, vol. 4, no. 2, pp. 399–410, Apr. 2012.

[29] M. A. Choma, M. V. Sarunic, C. Yang, and J. A. Izatt, "Sensitivity advantage of swept source and Fourier domain optical coherence tomography," *Opt. Express.*, vol. 11, pp. 2183–2189, 2003.

[30] R. Huber, M. Wojtkowski, K. Taira, J. Fujimoto, and K. Hsu, "Amplified, frequency swept lasers for frequency domain reflectometry and OCT imaging: design and scaling principles," *Opt. Express.*, vol. 13, pp. 3513–3528, 2005.

Yi Rao (S'08) received the B.S. and M.S. degrees in electronics engineering from Tsinghua University, Beijing, China, in 2005 and 2008, respectively. He is currently working toward the Ph.D. degree in electrical engineering and computer sciences at the University of California, Berkeley, USA.

His research interests include high-contrast gratings, vertical-cavity surface-emitting lasers, and integrated photonics.

Weijian Yang (S'09) received the B.S. degree in electronics engineering and computer science from Peking University, Beijing, China in 2008. He is currently working toward the Ph.D. degree in electrical engineering and computer sciences at the University of California, Berkeley, USA.

His research interests include high-contrast gratings, integrated photonics, vertical-cavity surface-emitting lasers, radio frequency photonics, and optical injection locking.

Mr. Yang is a student member of the Optical Society of America.

Christopher Chase received the B.E.E. degree from the University of Minnesota-Twin Cities, Minneapolis, USA, in 2005, and the Ph.D. degree from the University of California at Berkeley, Berkeley, USA, in 2011, all in electrical engineering. He investigated high-contrast grating integration in tunable and long-wavelength VCSELs in his dissertation research.

He is currently working on tunable long-wavelength VCSELs at Bandwidth10 in Newark, CA, USA.

Michael C. Y. Huang received the B.S. and Ph.D. degrees in electrical engineering and computer sciences from the University of California, Berkeley, USA, in 2002 and 2007, respectively.

He is currently working on tunable long wavelength VCSELs at Bandwidth10 in Newark, CA. His current research interests include nanostructured materials, nano- and microsemiconductor optoelectronic devices, and their applications.

D. Philip Worland is the President and founder of Bandwidth10, Inc., San Jose, CA USA (2011 to present), where has been focusing on developing and bring to market innovative VCSEL technology for high speed data applications. He was with Worland Consulting (2002 to present), with Vuemetrix, Inc. (2002 to 2004), with Bandwidth9, Inc. (1998 to 2002) as the CEO and President, with SDL, Inc. (1983 to 1998) as the Sr. Executive Vice President of Operations, and with Exxon Office Systems OIS (Optical Information Systems, Inc.) (1979–1983) as the Director of Operations. He holds 14 patents in opto-electronics.

Salman Khaleghi received the B.Sc. degree in electrical engineering from the Sharif University of Technology, Tehran, Iran, in 2007, and the M.Sc. degree from the University of Southern California (USC), Los Angeles, USA, where he is currently working toward the Ph.D. degree in electrical engineering.

From 2006 to 2007, he was a Researcher at Optical Networks Research Laboratory, Sharif University of Technology. He has been a Research Member of the USC Optical Communications Laboratory and Information Sciences Institute since 2007 and 2012, respectively. He is a Reviewer of the journals *Optics Express*, *Optics Letters*, *Applied Optics*, *Journal of Lightwave Technology*, and the IEEE PHOTONICS JOURNAL. He is the author or coauthor of more than 30 peer-reviewed journal articles and conference papers. His research interests include the study and application of advanced modulation formats and of nonlinear optical signal processing for applications to optical communication systems.

Mr. Khaleghi is a student member of the IEEE Photonics Society, the IEEE Communications Society, and the Optical Society of America. He received the USC Viterbi School of Engineering Doctoral Fellowship Award.

Mohammad Reza Chitgarha received the B.S. degrees from the Sharif University of Technology, Tehran, Iran, in 2008. He is currently working toward the Ph.D. degree in electrical engineering at the University of Southern California, Los Angeles, USA.

His research interests include optical signal processing, advanced modulation formats and coherent detection for optical communications, optical performance monitoring, and optical data communication networks. He is the author or coauthor of more than 30 peer-reviewed journal articles and conference papers. He is a reviewer of the *Optics Letter* and the IEEE/OSA JOURNAL OF LIGHTWAVE TECHNOLOGY.

Prof. Chitgarha is a student member of the IEEE Communication Society and the Optical Society of America.

Morteza Ziyadi was born in Iran in 1986. He received the B.S. and M.S. degrees (with Hons.) in electrical engineering from the Iran University of Science and Technology, Tehran, Iran, in 2008 and the Sharif University of Technology, Tehran, in 2010, respectively. He is currently working toward the Ph.D. degree in the Department of Electrical Engineering, University of Southern California (USC), Los Angeles, USA.

Since fall 2011, he has been a member of Optical Communication Lab at USC. His research interests include optical signal processing, advanced modulation formats in optical communication systems, optical CDMA and OFDM.

Alan E. Willner (F'04) received the B.A. degree in physics from Yeshiva University, New York, NY, USA, in 1982 and the Ph.D. degree in electrical engineering from Columbia University, New York, NY, USA, in 1988. He received an Honorary Degree, Honoris Causa, from Yeshiva University, New York, NY, USA, in 2012.

He was at AT&T Bell Labs and Bellcore, and is currently the Steven and Kathryn Sample Chair in Engineering at the University of Southern California, Los Angeles, USA. He has coauthored more than 900 publications, including one book and holds 24 patents.

Dr. Willner is an International Fellow of the U.K. Royal Academy of Engineering and a Fellow of the American Association for the Advancement of Science (AAAS), the Optical Society of America (OSA), and The International Society for Optics and Photonics (SPIE). His professional activities include: the Co-Chair of the U.S. National Academies Study on Harnessing Light II, the President of the IEEE Photonics Society, the Editor-in-Chief of the IEEE/OSA JOURNAL OF LIGHTWAVE TECHNOLOGY, the Editor-in-Chief of *OSA Optics Letters*, the Editor-in-Chief of the IEEE JOURNAL OF SELECTED TOPICS IN QUANTUM ELECTRONICS, the Co-Chair of the OSA Science and Engineering Council, the General Co-Chair of the Conference on Lasers and Electro-Optics (CLEO), the Chair of the IEEE TAB Ethics and Conflict Resolution Committee, the General Chair of the IEEE Photonics Society Annual Meeting, and the Program Co-Chair of the OSA Annual Meeting. He received the National Science Foundation (NSF) Presidential Faculty Fellows Award from the White House, the Packard Foundation Fellowship, the Guggenheim Foundation Fellowship, the NSF National Young Investigator Award, the Fulbright Foundation Senior Scholars Award, the OSA Forman Engineering Excellence Award, the OSA Leadership Award, the IEEE Photonics Society Engineering Achievement Award, the IEEE Photonics Society Distinguished Traveling Lecturer Award, the USC University-Wide Associates Award for Creativity in Research, the USC University-Wide Associates Award for Excellence in Teaching, and the Eddy Award from Pennwell for the Best Contributed Technical Article.

Connie J. Chang-Hasnain (M'88–SM'92–F'98) received the Ph.D. degree from the Electrical Engineering and Computer Sciences Department, University of California at Berkeley, Berkeley, USA, in 1987.

She was a Technical Staff Member at Bellcore (1987–1992), She was an Assistant Professor (1992–1995), and an Associate Professor (1995–1996) of Electrical Engineering at Stanford University. She is currently the John R. Whinnery Chair Professor in the Department of Electrical Engineering and Computer Sciences and the Chair of the Nanoscale Science and Engineering Graduate Group at the University of California at Berkeley. She is a Visiting Professor of Peking University (China) and National Jiao Tung University (Taiwan). Her research interests include new optical structures and materials for integrated optoelectronics.

Dr. Chang-Hasnain was a member of the USAF Scientific Advisory Board and the Board on Assessment of NIST Programs, the National Research Council. She was the General Co-Chair of the 1999 Conference on Lasers and Electro-Optics, the 2005 Asia Pacific Optical Communications Conference, the 2007 OSA Slow and Fast Light Topical Meeting, the 2007 OSA Frontiers in Optics Conference, and the 2012–2013 Co-Chair of the High-Contrast Metastructures Conference in SPIE Photonics West. She served as an IEEE LEOS Board of Governor and an OSA Director-at-Large. She was the Editor-in-Chief of the *Journal of Lightwave Technology* (2007–2012). She is an Honorary Member of the A.F. Ioffe Institute (Russia) and the Chang Jiang Scholar Endowed Chair at Tsinghua University (China). She has been awarded with the 2011 IEEE David Sarnoff Award for pioneering contributions to vertical-cavity surface-emitting laser (VCSEL) arrays and tunable VCSELs; the 2007 Optical Society of America (OSA) Nick Holonyak Jr. Award; the 2009 Japan Society of Applied Physics Microoptics Award; the 2009 Guggenheim Memorial Foundation Fellowship; and the 2009 Humboldt Research Award. She was awarded with the 2008 National Security Science and Engineering Faculty Fellowship by the Department of Defense.